PNAS RESEARCH ARTICLE | APPLIED PHYSICAL SCIENCES PLANT BIOLOGY

Phycobilisome core architecture influences photoprotective quenching by the Orange Carotenoid Protein

Ayesha Ejaz[a], Markus Sutter[b,c,d], Sigal Lechno-Yossef[b], Cheryl A. Kerfeld[b,c,d,e], and Allison H. Squires[f,g,h,i,1]

Affiliations are included on p. 10.

Edited by Martin Gruebele, University of Illinois Urbana-Champaign, Urbana, IL; received October 3, 2024; accepted August 11, 2025

Photosynthetic organisms rely on sophisticated photoprotective mechanisms to prevent oxidative damage under high or fluctuating solar illumination. Cyanobacteria, which have evolved a unique, water-soluble light-harvesting complex—the phycobilisome—achieve photoprotection through a photoactivatable quencher called the Orange Carotenoid Protein (OCP). Phycobilisomes are highly symmetric and modular, formed by hierarchical assembly of conserved subunits into diverse geometries ranging from simple bundles to elaborate fan- or bouquet-like macromolecular architectures. Although OCP is known to provide photoprotection across species of cyanobacteria with different phycobilisome structures, it is not known whether or how these structural variations relate to changes in the photoprotective function of OCP. For example, OCP was recently discovered to bind as a dimer at two specific instances of an abundant structural motif on the tricylindrical phycobilisome of *Synechocystis* sp. PCC 6803, yet these sites are sterically inaccessible on a more common pentacylindrical phycobilisome (*Anabaena* sp. PCC 7120). To understand how structural modularity and binding specificity contribute to conservation of OCP binding sites and function across different phycobilisome architectures, here we compare experimentally measured photophysical states accessible to these prototypical tricylindrical and pentacylindrical phycobilisomes, with and without OCP, at the single-molecule level. Together with Monte Carlo simulations of exciton transfer in OCP-quenched phycobilisomes, our results suggest that OCP binds at distinct and specific sites in each type of phycobilisome, yet provides nearly identical quenching strength to both phycobilisomes. Our findings highlight the utility of modular phycobilisome structures in balancing robust conservation of photoprotective function with adaptability of site-specific binding across species.

photosynthesis | phycobilisome | Orange Carotenoid Protein | single-molecule spectroscopy | ABEL trap

Significance

Among photosynthetic organisms, cyanobacteria deploy uniquely modular solutions for both light harvesting and photoadaptation, resulting in macromolecular antenna complexes that have high subunit homology across species, but assemble into very different architectures. Here, we combine cutting-edge experimental approaches in single-particle fluorescence spectroscopy with structural analysis and computational simulations to reveal functional differences—and similarities—of how the Orange Carotenoid Protein provides photoprotection to phycobilisomes with different core architectures. Our results reveal that while binding sites and affinity for the Orange Carotenoid Protein differ across species, the quenching strength and mechanism appear to be conserved. This work therefore provides insights into the emergence of robust yet tunable adaptive functions in a highly symmetric, modular, and self-assembled macromolecular structure.

Sunlight drives photosynthesis and solar cells alike, but high light can create damage. Among light-harvesting organisms, cyanobacteria have evolved a unique light-harvesting antenna complex, the phycobilisome (1–4). Together with the photoswitchable Orange Carotenoid Protein (OCP) (5, 6), this complex has enabled survival across a wide range of environments and solar illumination. The macromolecular structures of phycobilisomes exhibit significant natural variation across species of cyanobacteria due to modular subunit composition, and at least some OCPs can quench phycobilisomes from different species, including across different phycobilisome architectures (7–10). However, the principles that govern nonphotochemical quenching of massive phycobilisomes (>6 MDa) by OCP (~34 kDa) remain poorly understood. Moreover, it is not clear to what extent OCP–phycobilisome quenching function—that is, the site(s) and strength of quenching—is conserved across cyanobacteria.

In different species of cyanobacteria, phycobilisome structures can be as simple as a cluster of rods or can take on more elaborate rod-core architectures with two to five core cylinders and six or more rods radiating outward, all held together via colorless linker proteins (11). Cylinders and rods are composed of stacked allophycocyanin hexamers and C-phycocyanin hexamers, respectively, and exhibit repeated structural motifs along their lengths with roughly threefold rotational symmetry. The arrangement of rods and cylinders funnels energy from more distal, blue-shifted pigments in the rods toward red-shifted pigments in the core, from which energy is transferred to a photosystem in the thylakoid membrane (12, 13). Only a handful of phycobilisome structures have been solved, including complexes with tricylindrical cores (14–18) and pentacylindrical cores (16, 19), two of the most common phycobilisome architectures (11, 20) (Fig. 1 *A* and *B*). OCP is present in most phycobilisome-containing cyanobacteria (21, 22). In the inactive "orange" form of OCP, a carotenoid spans the N- and C- terminal domains which are connected by a flexible

The authors declare no competing interest.

This article is a PNAS Direct Submission.

[1]To whom correspondence may be addressed. Email: asquires@uchicago.edu.

This article contains supporting information online at https://www.pnas.org/lookup/suppl/doi:10.1073/pnas.2420355122/-/DCSupplemental.

Published October 7, 2025.

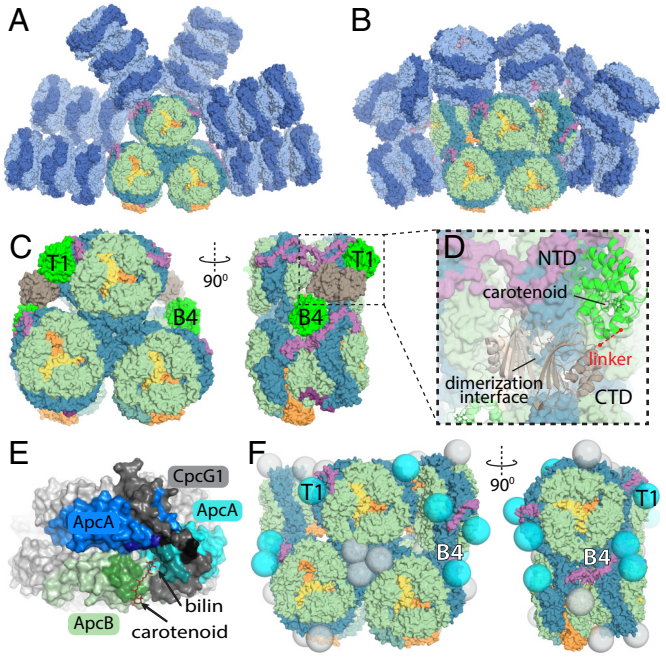

Fig. 1. Structure and OCP binding sites for phycobilisomes with tricylindrical and pentacylindrical cores. Cryo-EM structures of (*A*) *Synechocystis* PCC. 6803 phycobilisome with a tricylindrical core (tri-PBS; composite map from (17)) and (*B*) *Anabaena* PCC. 7120 phycobilisome with a pentacylindrical core [penta-PBS; PDB: 7EYD (16)]. In addition to the common allophycocyanin tricylindrical core, the penta-PBS core has two extra flanking core half-cylinders, and it has eight C-phycocyanin rods. (*C*) Cryo-EM structure of tri-PBS bound to tri-OCP [lime/tan; PDB: 7SC9 (17)] shows that four tri-OCP bind to the tri-PBS core as two dimers, with the N-terminal domain of each tri-OCP contacting a core cylinder at sites T4 and B4 (dimer 1) or T1′ and B4′ (dimer 2). Dimers are formed through the C-terminal domains. (*D*) Zoom on T1 binding site (dotted black box from panel *C*) showing the tri-OCP bound structure [PDB: 7SC9 (17)] with the N- (lime) and C-terminal domains (tan) separated and joined by a linker (red dotted, unstructured region data not available). A second tri-OCP can be seen at lower left, dimerized to the first via the C-terminal domains with near-C2 symmetry. (*E*) The consensus binding site of tri-OCP on tri-PBS occurs at a junction of three allophycocyanin monomers, interacting with one ApcB (green) and two ApcA subunits (cyan, blue) and peripherally interacting with the CpcG1 rod-core linker (dark gray) [top cylinder complex from PDB: 8TPJ (25)]. Residues within 3 Å of OCP are colored darker than their corresponding subunit color. The OCP (not pictured to avoid occluding view of the site) is located toward the viewer with only its carotenoid depicted (maroon sticks). (*F*) The penta-PBS core structure [PDB: 7EYD (16)] is shown with all identified instances of the OCP binding motif marked with spheres. Cyan spheres: sites without significant steric clashes. Light gray spheres: sites where OCP access would be blocked by a rod, another part of the core cylinder, or the underlying thylakoid membrane. The T1 site is labeled in black text, and the B4 site (occluded by the E cylinder) is labeled in white text.

peptide linker (23) (*SI Appendix,* Fig. S1). Upon illumination by blue-green light, the two halves separate into the activated "red" form, with the carotenoid burrowing into the N-terminal domain so that its transition dipole moment is tuned for quenching (24, 25). Activated OCP binds the phycobilisome (17) and dissipates excess energy as heat. Over decades, attempts to locate the OCP binding site on the phycobilisome using time-resolved fluorescence spectroscopy (26), site-directed mutagenesis (27), computational modeling (28), and single-molecule fluorescence spectroscopy (29, 30) arrived at the consensus that OCP binds to the phycobilisome core. Although candidate binding motifs appear frequently in core cylinders due to their highly symmetric subunit composition, previous experimental evidence suggested the presence of at most one (6) or two (30) bound OCPs on quenched phycobilisomes.

Recently, cryo-EM structures of an OCP-quenched tricylindrical-core phycobilisome (hereafter "tri-PBS") provided the first definitive insight into the structure of an OCP–phycobilisome complex (17). The structure shows two dimers of OCP bound at two pairs of sites in the tricylindrical core (Fig. 1*C*). Due to the C2 symmetry of the phycobilisome, there are only two structurally unique binding sites for OCP, one on the bottom cylinder, called site "B4", and one on the top cylinder, called site "T1" (see *SI Appendix,* Fig. S2 for site nomenclature). The N-terminal domains of each OCP in a dimer bind to sites B4 and T1 (or B4′ and T1′) and these domains are joined by the flexible linkers to their dimerized C-terminal domains (Fig. 1*D*). The same binding motif is present at both the B4 and T1 sites and involves a junction of three allophycocyanin monomers (Fig. 1*E*). Surprisingly, examination of the corresponding B4 and T1 locations revealed that this dimer binding site is unavailable on a pentacylindrical-core phycobilisome (hereafter "penta-PBS") (17): Only the T1 site is accessible on penta-PBS because compared to tri-PBS, penta-PBS has two additional rods as well as two additional core half-cylinders that sterically block the B4 site (Fig. 1*F*). Yet solution-phase data indicate that activated OCP exists as a dimer (31–34). Moreover, multiple reports using bulk assays have shown that the efficacy of cross-species quenching varies widely for different pairs of OCPs and phycobilisomes (7–10). Therefore, the available structural and biochemical evidence challenges the idea that OCP's quenching function may be conserved across cyanobacteria with different phycobilisome architectures.

Single-particle fluorescence spectroscopy allows us to compare OCP function across species of cyanobacteria, disentangling changes in quenching from changes in binding affinity or any underlying photophysical or structural differences among phycobilisomes. It enables characterization of individual photophysical states without ensemble averaging or synchronization, revealing population-wide or dynamic heterogeneities underpinning molecular function, which are obscured in bulk assays. The handful of single-particle studies performed to date on tri-PBS and OCP–tri-PBS interactions have discovered photoresponsive dynamics both at the level of individual phycobiliprotein subunits (35–37) and for the entire phycobilisome (30, 38, 39). These studies have also revealed two distinct quenched states caused by OCP, called "Q1" and "Q2", binding, which represent binding of one or two OCP dimers, respectively (30), as well as evidence of transition states during OCP binding (29). Such single-particle measurements of the properties and distributions of discrete photophysical states can be compared to computational models based on established molecular structures and bulk ultrafast measurements of energy transfer (40, 41) to establish the molecular mechanisms governing OCP quenching of phycobilisomes.

Here, we measure and compare OCP–phycobilisome quenching function (quenching strength and binding sites) across two cyanobacterial species with different phycobilisome core architectures, one prototypical tri-PBS [*Synechocystis* sp. PCC 6803; (17)] and one prototypical penta-PBS [*Anabaena* sp. PCC 7120; (16, 19)]. To distinguish the effects of quenching function from binding affinity and structural heterogeneity, we employ single-particle experiments in an Anti-Brownian ELectrokinetic (ABEL) trap (42, 43) where we use OCP-quenched states of tri-PBS as a reference for penta-PBS experiments to establish conserved (and nonconserved) quenched states between the two systems. We then use photon-by-photon Monte Carlo simulations of exciton transfer through compartmentalized models of the phycobilisomes (40, 41) to identify the penta-OCP binding sites and quenched states that best fit our empirical spectroscopic data. Our results show that features such as dimeric OCP binding and OCP quenching strength are conserved across both species. The integration of structural, experimental, and simulation results enables us to

propose a binding model for OCP on penta-PBS where two dimers bind at the T1/E3 sites. Finally, penta-OCP quenches both penta-PBS and tri-PBS to the same photophysical states, but this cross-species compatibility is not reciprocated by tri-OCP, indicating that details of the binding interface may influence binding specificity without altering OCP function. Together, our findings suggest that the quenching mechanism of OCP is likely preserved across the two phycobilisome architectures, even as the modular nature of the phycobilisome facilitates quenching at different sites.

Results

Sequence and Structure Similarity of Tri- and Penta-PBS and OCP. We selected two commonly studied species of cyanobacteria for which the phycobilisome structure and OCP structures are available, *Synechocystis* sp. PCC 6803 (tri-PBS) and *Anabaena* sp. PCC 7120 (penta-PBS). Both species possess OCP from the OCP1 family, the most common form among OCP paralogs including OCP1, OCP2, and OCP3 (10, 44). Hereafter, we will refer to OCP1 from *Synechocystis* sp. PCC 6803 as "tri-OCP" and OCP1 from *Anabaena* sp. PCC 7120 as "penta-OCP". The crystal structures of tri-OCP and penta-OCP in the inactive state align with an RMSD of 0.34 Å (*SI Appendix*, Fig. S1), and the sequences of their N-terminal domains are 84% identical (*SI Appendix*, Note S1 and Fig. S3), confirming a high degree of structure and sequence similarity between tri-OCP and penta-OCP.

To verify that the tri-PBS and penta-PBS used in this study are representative of their respective phycobilisome architectures, we compared the sequences of their allophycocyanin (core) subunits to those of other tri- and pentacylindrical phycobilisomes (tricylindrical: *Synechococcus* sp. PCC 7002; pentacylindrical: *Halothece* sp. PCC 7418) and found that the sequences were 87 and 89% identical, respectively. Finally, we confirmed that allophycocyanin is also well-conserved between our tri-PBS and penta-PBS, with 83% sequence identity (*SI Appendix*, Fig. S4).

Without additional structural or sequence information to suggest plausible binding sites for penta-OCP or possible changes in function, we turn to single-particle experiments, using OCP-quenched states of tri-PBS as a reference for penta-PBS experiments, combined with simulations to establish a binding model for OCP on penta-PBS.

Single Phycobilisome Measurements. The ABEL trap allows us to observe single phycobilisomes for long timescales without immobilizing or tethering them to a surface, thereby minimizing perturbations that could affect protein complex structure, energy transfer pathways, or OCP binding. The ABEL trap uses closed-loop feedback voltages to maintain the position of a single phycobilisome in free solution while monitoring its fluorescence. For each trapped molecule, we measure fluorescence brightness, lifetime, and the ratio of emitted light >660 nm to total brightness, here called the "red ratio" (*Materials and Methods* and *SI Appendix*, Figs. S5 and S6). Together, these parameters enable us to distinguish among different types of trapped particles—including unquenched phycobilisomes with different architectures, various quenched states of the phycobilisome, C-phycocyanin rods, and smaller phycobilisome subunits—and their photophysical states. Specifically, we ask whether tri-PBS and penta-PBS exhibit similar quenched states, whether penta-PBS-quenched states are also dictated by the number and dimerization of bound penta-OCP, and how previously reported cross-species quenching (7–10) manifests at the single-molecule level.

In the absence of OCP, both tri-PBS and penta-PBS largely populated the spectroscopic state associated with emission of a single pristine phycobilisome (Fig. 2 *A* and *B*), with some higher-order oligomers present that were filtered out during analysis (*SI Appendix*, Note S2 and Figs. S7 and S8). We used these pristine states to confirm sample quality and to benchmark the relative cross sections, i.e., rod lengths, of each sample (*SI Appendix*, Note S3). As expected, fluorescence lifetime (1.70 ± 0.10 ns) and red ratio (0.78 ± 0.02) in the pristine state were nearly identical for both types of pristine phycobilisomes (Table 1). We attribute small deviations in individual phycobilisome-to-phycobilisome brightness to variability of rod lengths. Notably, raw data traces reveal

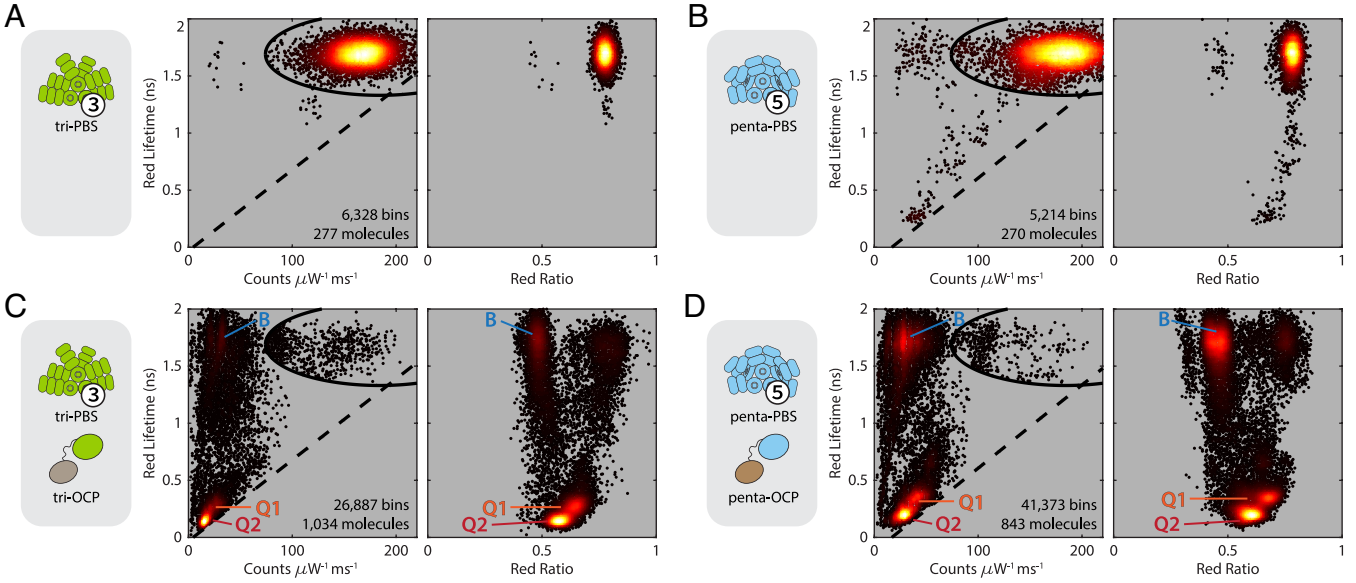

Fig. 2. Photophysical states of unquenched and OCP-quenched phycobilisomes with tricylindrical and pentacylindrical cores. (*A*) Projections of red lifetime vs. brightness (*Left*) and red lifetime vs. red ratio (*Right*) for tri-PBS only are shown as scatter heatmaps, with points colored according to relative density. Each point represents a 500-photon bin for which the photophysical parameters were calculated. Red lifetime refers to the lifetime calculated from photons detected by the red channel. Data from phycobilisome oligomers were filtered out (black oval; black dotted line; see *Materials and Methods* and *SI Appendix*, Note S2 and Figs. S7, S8 and S13–S15). Heatmaps for (*B*) penta-PBS only, (*C*) tri-PBS quenched by tri-OCP, and (*D*) penta-PBS quenched by penta-OCP are also presented. Quenched populations Q1 (orange) and Q2 (red), as well as the rod population B (blue), are labeled for all panels in which they appear.

Table 1. Mean and SD of measured parameters for unquenched, quenched, and rod populations from experiments for OCP-quenched phycobilisomes

Phycobilisome	OCP	State	Brightness (counts ms^{-1} μW^{-1})	τ Red channel (ns)	τ Green channel (ns)	Red ratio
Synechocystis PCC. 6803 (tricylindrical; tri-PBS)	No OCP	Unquenched	167 ± 20	1.70 ± 0.09	1.32 ± 0.11	0.775 ± 0.023
	Synechocystis PCC. 6803 (tri-OCP)	Q1	25.0 ± 5.1 (15%)	0.28 ± 0.04	0.20 ± 0.03	0.645 ± 0.032
		Q2	15.9 ± 3.0 (9.5%)	0.15 ± 0.03	0.11 ± 0.03	0.577 ± 0.032
		Rods	29.0 ± 7.2	1.72 ± 0.14	1.67 ± 0.12	0.482 ± 0.026
	Anabaena PCC. 7120 (penta-OCP)	Q1	19.4 ± 4.9 (12%)	0.28 ± 0.04	0.21 ± 0.03	0.640 ± 0.034
		Q2	12.23 ± 3.0 (7%)	0.16 ± 0.03	0.11 ± 0.03	0.578 ± 0.034
		Rods	20.6 ± 6.3	1.68 ± 0.15	1.61 ± 0.15	0.486 ± 0.027
Anabaena PCC. 7120 (pentacylindrical; penta-PBS)	No OCP	Unquenched	181 ± 26	1.70 ± 0.10	1.34 ± 0.13	0.783 ± 0.023
	Anabaena PCC. 7120 (penta-OCP)	Q1	40.5 ± 6.6 (22%)	0.35 ± 0.04	0.24 ± 0.03	0.673 ± 0.034
		Q2	28.4 ± 5.6 (16%)	0.21 ± 0.04	0.14 ± 0.03	0.597 ± 0.036
		Rods	29.3 ± 7.9	1.71 ± 0.11	1.66 ± 0.11	0.453 ± 0.036
	Synechocystis PCC. 6803 (tri-OCP)	Unquenched	159 ± 24	1.66 ± 0.10	1.47 ± 0.11	0.775 ± 0.022
		Q1 (possible)	36.6 ± 9.0 (21%)	0.36 ± 0.08	0.25 ± 0.04	0.656 ± 0.043
		Rods	24.2 ± 6.3	1.72 ± 0.11	1.68 ± 0.11	0.447 ± 0.030

that each phycobilisome displays consistent photophysical parameters while trapped, confirming that the ABEL trap does not perturb the structure of trapped phycobilisomes and that the low excitation laser power used here does not induce photophysical dynamics or damage (*SI Appendix,* Figs. S9 and S10). Note that without OCP, higher laser powers cause photobleaching from the pristine state over time (*SI Appendix,* Figs. S11 and S12).

OCP-Quenched Photophysical States in Tri-PBS and Penta-PBS. We established the OCP-quenched states of tri-PBS, for which the exact binding sites are known (17), as a reference for comparison to quenching in penta-PBS. We trapped single tri-PBS complexes in the presence of activated tri-OCP, illuminated at high laser power in the ABEL trap, and examined the resulting photophysical states (*Materials and Methods*; see also *SI Appendix*, Note S2 and Figs. S13–S15). In agreement with previous reports (30), quenched tri-PBS complexes exhibited three distinct photophysical states in addition to the pristine state (Table 1; Fig. 2*C*). One is a dim, long-lifetime, and highly blue-shifted state, B, likely corresponding to detached rods. Two OCP-quenched states, Q1 and Q2, are dim and blue-shifted with short lifetimes (Table 1; see also *SI Appendix*, Note S3). In the context of the known structure of the tricylindrical phycobilisome–OCP complex, we assign Q1 as a state where one OCP dimer is bound at T1 and B4, and Q2 as the fully quenched state with two OCP dimers bound at T1/B4 and T1′/B4′ (17).

We expected that OCP-quenched penta-PBS might exhibit shifted, or different numbers of, quenched states as site B4 is sterically blocked in the penta-PBS cryo-EM structure. Surprisingly, penta-PBS quenched by penta-OCP produced three photophysical states that appeared to correspond almost exactly to the B, Q1, and Q2 states observed for the quenched tri-PBS (Table 1; Fig. 2*D*). For penta-PBS, the Q1 and Q2 states have nearly identical lifetimes and red ratios compared to tri-PBS Q1 and Q2 but are slightly less quenched than in the tri-PBS. This slight difference in brightness between the two species could be attributable to differences in the binding site(s) or quenching strength of OCP or underlying differences in the phycobilisome structures and energy transfer pathways; our results and simulations support the latter explanation (vide infra). Specifically, since penta-PBS has more rod cross-section and a slower rod-to-core exciton transfer rate than tri-PBS (41), a higher proportion of rod fluorescence might be expected in quenched penta-PBS even if OCP quenching function is identical.

Dimerization and Number of Bound Tri-OCP and Penta-OCP. For tri-PBS, it has been previously established that Q1 and Q2 represent binding of one or two tri-OCP dimers, respectively (17, 30). To verify that Q1 and Q2 on penta-PBS are also produced by different numbers of bound penta-OCP, rather than by different quenching sites, we titrated penta-OCP with penta-PBS (*SI Appendix,* Fig. S16*A*). In the presence of excess activated penta-OCP, most penta-PBS were found in the Q2 state. As the OCP concentration was reduced, the quenched population shifts to favor the Q1 state. Together, these data indicate that Q1 and Q2 are likely produced by increasing numbers of penta-OCP bound to penta-PBS, similar to tri-OCP quenching of tri-PBS.

We next eliminated dimerization in tri-OCP and penta-OCP, to establish whether the monomeric form 1) quenches the phycobilisome and/or 2) produces new, less-quenched states compared to Q1 and Q2. Previous work has shown that the N- and C-terminal domains of OCP can be cleaved using a protease and that the resulting N-terminal domain, called red carotenoid protein (RCP), can quench the phycobilisome (8). Without the C-terminal domain, the RCP is constitutively active and the potential for dimerization is lost. We generated cleaved versions of both OCPs, referred to here as tri-RCP and penta-RCP, respectively, and verified bulk quenching of both types of phycobilisomes by these RCPs (see *SI Appendix,* Figs. S17 and S18 for unquenched and quenched bulk spectra for all four phycobilisome-OCP and phycobilisome-RCP combinations). We repeated the single-molecule quenching assays—using higher RCP concentrations than for OCP, as RCP unbinds at the low concentrations needed for single-molecule measurements (*SI Appendix,* Fig. S19)—and observed new, less-quenched states for both tri-PBS and penta-PBS (Table 2):

For tri-PBS quenched by tri-RCP, we observed just one new, less quenched state, labeled Qa (Fig. 3*A*). Even with a large excess of tri-RCP, we observed neither Q1 nor Q2; a slight tail on Qa encroaches toward Q1, but it is not clear whether this population represents a separate quenched state. This result suggests that in tri-PBS, the dimerization of OCP through interaction of the C-terminal domains is necessary for binding and/or quenching.

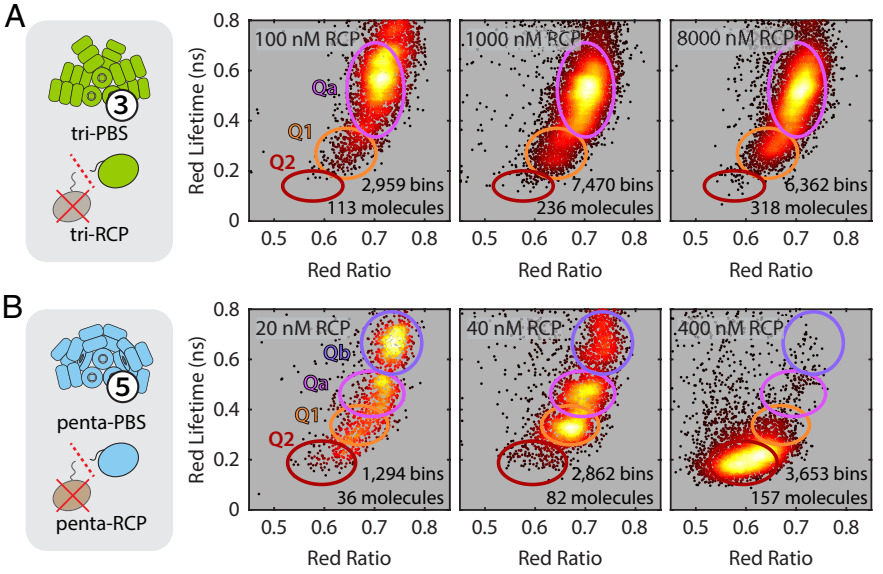

Fig. 3. Titrations of phycobilisomes with the constitutively active red carotenoid protein (RCP). (*A*) Scatter heatmaps for tri-PBS quenched by tri-RCP show that even at high concentrations of tri-RCP (*Right*), the Q2 (red ellipse) state is not observed and relatively few phycobilisomes visit the Q1 (orange ellipse) state. As the amount of RCP is reduced (center, *Left*), most phycobilisomes remain in a newly emerged, less quenched state, labeled Qa (pink ellipse). (*B*) Scatter heatmaps for penta-PBS quenched by penta-RCP show that at high concentrations of penta-RCP (*Right*), penta-PBS can be fully quenched to the Q2 state. As the amount of RCP is reduced (center, *Left*), the population shifts to less-quenched states including two new states, Qa (pink ellipse) and Qb (purple ellipse). The Qa state is similar for both tri- and penta-PBS, but Qb is only observed for penta-PBS. Throughout: each point represents a 500-photon bin. Points are colored according to relative density of each scatter plot.

In contrast, titrating penta-PBS with penta-RCP revealed at least four distinct quenched populations including Q1, Q2, and two new, less-quenched states, Qa and Qb (Fig. 3*B*). At the highest concentrations of RCP, penta-PBS was quenched to the Q2 photophysical state that was originally observed using the full OCP. Lowering the amount of RCP generated the Q1 state as well as the two less-quenched populations, Qa and Qb, where Qa is more quenched than Qb. Since the Qa and Qb states, which are less quenched than Q1 and Q2, are only observed the obligatory monomer RCP, we conclude that these additional states are produced by single RCPs binding and quenching the phycobilisome. The appearance of two new populations in the case of penta-PBS suggests that there are at least two sites at which penta-RCP or monomers of penta-OCP may bind.

Cross-Species Quenching by Tri-OCP and Penta-OCP. Cross-species quenching efficacy as measured by bulk assays is known to vary widely for different OCP–PBS pairs (7–10). Jallet et al. reported that the tri-OCP used in the present work failed to quench phycobilisomes from *Synechococcus* PCC 7942 (bicylindrical core) and *Arthrospira platensis* PCC 7345 (tricylindrical core), and achieved ~20% quenching on *Anabaena variabilis* (pentacylindrical core, closely related to the penta-PBS from this present work) (7). The same tri-PBS, on the other hand, can be quenched by the *Arthrospira* OCP (7) as well as RCP (8), by penta-OCP (9), and even by representatives from other families of OCP (10). To separate out the degree of cross-species quenching from changes in binding affinity, which could reveal conservation or alterations in quenching function, here we measured the photophysical states generated by cross-species quenching at the single-particle level.

Quenching of tri-PBS by activated penta-OCP produced two states closely corresponding to Q1 and Q2 (Table 1; Fig. 4*A*). Here, both Q1 and Q2 are slightly dimmer (12% and 7% brightness, respectively) than for the native tri-OCP, but the lifetimes and red ratios are nearly identical. We also note that although the penta-OCP fully quenches both types of phycobilisomes, it appears to have slightly higher affinity for its native penta-PBS than for the tri-PBS (79% Q2 vs. 65% Q2 at ~1:100 phycobilisome:OCP, *SI Appendix*, S16*B*). In contrast, we did not observe quenched populations when activated tri-OCP was added to the penta-PBS (Fig. 4*B*; Table 1), in agreement with previous bulk reports (7). In monomer (N-terminal domain/RCP) cross-species experiments, tri-PBS quenched with penta-RCP exhibited only population Qa regardless of RCP concentration (Fig. 4*C*), supporting functional similarities (i.e.: dimerization and binding sites) between tri-OCP and penta-OCP. As with tri-OCP, the tri-RCP did not quench penta-PBS.

Altogether, the observed one-way compatibility and preservation of quenched state properties indicate that even though penta-OCP can access, bind, and quench tri-PBS, the tri-OCP does not have access to the penta-PBS binding sites, cannot bind to them, or can access and bind but does not quench. Further, the monomer results indicate that the cross-species asymmetry is not a consequence of tri-OCP dimerization, but rather that the tri-OCP N-terminal domain simply cannot interact with the penta-PBS in the same way as the penta-OCP N-terminal domain. In our computational model below, we determine, among other questions, whether penta-OCP interacts with the tri-PBS at the same sites as the tri-OCP or by a different combination of binding sites and quenching rate(s) that simply happen to produce the same number and photophysical properties of quenched states as the native tri-OCP.

Connecting OCP Binding and Quenching Function to Phycobilisome Structure. Our experimental results point to certain functional similarities (dimerization, possible binding sites) between tri-OCP and penta-OCP, but also reveal differences in their function as monomers, including differences in the number of RCP-quenched states between the tri- and penta-cylindrical phycobilisome complexes. Here, we quantitatively evaluate multiple plausible quenching scenarios that could give rise to these observations and determine the extent to which

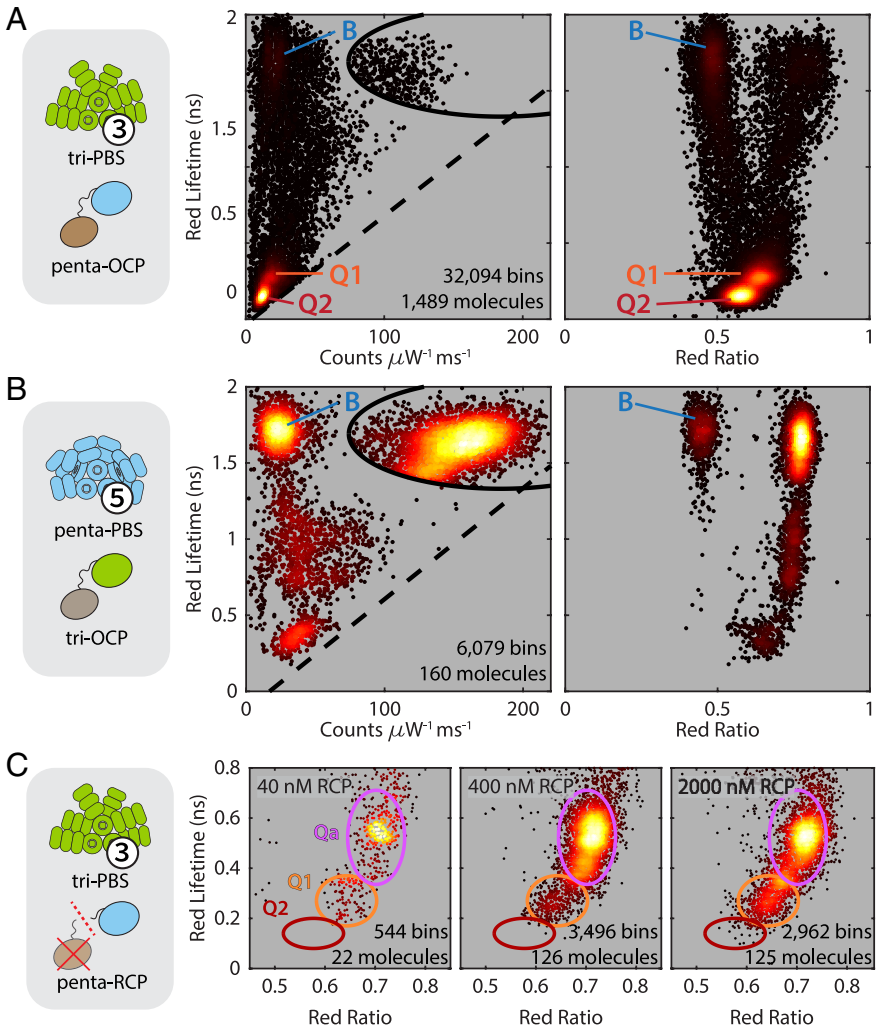

Fig. 4. Cross-species quenching with OCP and RCP. (*A*) Scatter heatmaps for tri-PBS quenched by penta-OCP and (*B*) penta-PBS quenched by tri-OCP are shown as scatter heatmaps, with points colored according to relative density. Quenched populations Q1 (orange) and Q2 (red), as well as the rod population B (blue), are labeled for all panels in which they appear. (*C*) Scatter heatmaps for cross-species quenching of tri-PBS titrated with penta-RCP show the same two states that were observed for quenching of tri-PBS by its own tri-OCP: Q1 (orange ellipse), and Qa (pink ellipse). Like tri-RCP, even at high concentration (*Right*) penta-RCP does not quench tri-PBS to state Q2 (red ellipse). Throughout: each point represents a 500-photon bin. Points are colored according to relative density of each scatter plot.

OCP–phycobilisome quenching function is conserved across the two complexes. We first identify all potential OCP binding sites on tri-PBS and penta-PBS. We then develop computational models of both tri-PBS and penta-PBS and use simulations to identify the OCP binding sites and quenching strengths that best fit our empirical spectroscopic data.

Potential OCP binding sites. The recently reported structure of the tricylindrical phycobilisome–OCP complex clearly shows that only sites T1 and B4 on tri-PBS bind the dimer of tri-OCP (17); however, the binding motif at these sites is abundant on the tri-PBS structure, appearing in 16 symmetrically unique locations (32 total). Of these sites, most are blocked by other parts of the

Table 2. Mean and SD of extracted parameters of observed quenched states from experiments for RCP-quenched phycobilisomes

Phycobilisome	RCP	State	Br (counts ms^{-1} μW^{-1})	τ Red channel (ns)	τ Green channel (ns)	Red ratio
Synechocystis PCC. 6803 (tricylindrical; tri-PBS)	*Synechocystis* PCC. 6803 (tri-RCP)	Qa	41.3 ± 9.5 (25%)	0.524 ± 0.085	0.392 ± 0.092	0.708 ± 0.023
	Anabaena PCC. 7120 (penta-RCP)	Qa	45.6 ± 9.7 (27%)	0.520 ± 0.079	0.391 ± 0.087	0.709 ± 0.022
Anabaena PCC. 7120 (pentacylindrical; penta-PBS)	*Anabaena* PCC. 7120 RCP (penta-RCP)	Qb	80.6 ± 11 (45%)	0.661 ± 0.05	0.511 ± 0.07	0.737 ± 0.020
		Qa	59.4 ± 8.4 (33%)	0.457 ± 0.04	0.330 ± 0.06	0.697 ± 0.025
		Q1	46.5 ±7.4 (26%)	0.336 ± 0.04	0.248 ± 0.05	0.670 ± 0.024
		Q2	28.3 ± 5.4 (16%)	0.195 ± 0.03	0.148 ± 0.04	0.598 ± 0.031

tri-PBS structure, or by the thylakoid membrane in situ; only four are not blocked (sites T1, T3, B4, and B9). We evaluated the similarity of each site to the consensus binding motif according to the RMSD of the aligned structures and found that the known binding sites and one unbound sites are highly similar (T1: 0.42 Å, B4: 0.800 Å, T3: 0.722 Å) while the other unbound site shows larger deviation (B9: 1.794 Å). For comparison, the RMSDs of the same set of sites in two different tri-PBS structures (PCC 6803 and PCC 7002) are nearly identical in all instances, further confirming that the PCC 6803 phycobilisome used in this work is a representative tri-PBS structure. While it is not clear why T3 and B9 on tri-PBS do not bind tri-OCP, it is likely that either structural variations at the binding interface confer strong site specificity, or that the positions and orientations of these sites may not be conducive to binding OCP dimers. See *SI Appendix*, Note S1 and Fig. S20 for description of motif alignment and determination of site availability, *SI Appendix,* Figs. S21 and S22 for motif locations on tri-PBS, and *SI Appendix,* Tables S1 and S2 for site availability and RMSD.

We identified 22 symmetrically unique instances (44 total) of the same binding motif on the penta-PBS core [PDB: 7EYD (16)]. Of these, only 7 sites (14 total) are not sterically blocked and could in principle accommodate an OCP N-terminal domain; two on the bottom cylinder (B1, B9), two on the top cylinder (T1, T3), and three on the extra half-cylinder (E2, E3, and E5) (Fig. 1*F*). Of these, T1, T3, and B1 align with the consensus binding site to within an RMSD of 1 Å (T1: 0.68 Å, T3: 0.89 Å, B1: 0.95 Å) while B9 and all three sites on the E cylinder have RMSDs over 1 Å (B9: 2.25 Å, E2: 1.21 Å, E3: 1.21 Å, and E5: 1.17 Å). As previously reported (17), the B4 site, which is available in tri-PBS to bind tri-OCP, is completely blocked by the E half-cylinder in penta-PBS. However, the T1 site remains accessible in both tri- and penta-PBS, making it a strong candidate for binding of penta-OCP. See also *SI Appendix*, Note S1, Figs. S20 and S23, and Tables S1 and S2.

Monte Carlo simulations. Following previous modeling efforts (30, 40), we elected to run compartmental Monte Carlo simulations of energy transfer in the phycobilisomes (Fig. 5 *A* and *B*) where equilibration within each compartment is assumed to be very fast relative to energy transfer between compartments, and rate constants are derived from ultrafast measurements (40, 41) (see *SI Appendix*, Note S4 for full simulation details and *SI Appendix,* Figs. S24 and S25 for model geometries and rates). We used these models to predict how different OCP binding sites, phycobilisome-OCP stoichiometry, and OCP quenching rates would influence the experimentally observed quenched states.

We benchmarked our simulations using the tri-PBS model with four OCPs arranged as two dimers bound to the known binding sites, so that one OCP from each dimer quenched a top core cylinder compartment and one OCP from each dimer quenched a bottom cylinder compartment, in agreement with the cryo-EM structures (17). As the true rate of OCP quenching is not known, we simulated a range of possible OCP quenching rates under the assumption that all four OCPs quench with identical strength. The predicted quenched states for one bound OCP dimer (Q1), two bound OCP dimers (Q2), and one bound OCP monomer (Qa) become more quenched at faster OCP quenching rates (Fig. 5*C*). We found that a quenching rate of 31 ns^{-1} correctly reproduced the experimentally observed properties of states Q2, Q1, and Qa for two dimers, one dimer, or one RCP, respectively.

Other combinations of two and four binding sites on tri-PBS produce states that are remarkably similar to Q1 and Q2 (Fig. 5*C* and *SI Appendix,* Fig. S26), respectively. The notable exceptions are the $T_{front}T_{back}$ (two OCPs bound, top cylinder only) and $B_{front}B_{front}$' (two OCPs bound, bottom of one phycobilisome face only) combinations, which produce a state that is less quenched than Q1 but more quenched than Qa. When only one OCP is present (binding of RCP or a monomer), state Qa is predicted regardless of which core compartment is quenched. Together, the results of these tri-PBS simulations establish an approximate quenching rate of 31 ns^{-1} for the tri-OCP monomer, validate the interpretation of Q1 and Q2 as one and two bound OCP dimers, respectively, and support the hypothesis that state Qa is generated by a single RCP.

The same Qa state was observed for penta-RCP binding to tri-PBS, suggesting that penta-RCP may quench with a similar rate to tri-RCP, and by extension, that penta-OCP may quench with a similar rate to tri-OCP. Our experimental observation of only Q1 and Q2 (and not Qa) for penta-OCP on tri-PBS also supports the idea that just like tri-OCP, penta-OCP binds as a dimer rather than a monomer to tri-PBS. We suggest, therefore, that the binding sites for penta-OCP on tri-PBS are likely, albeit not proven, to be identical to tri-OCP. Most importantly, these cross-species results establish that the quenching mechanisms of tri-OCP and penta-OCP when acting on tri-PBS are likely to be the same.

We next simulated combinations of penta-OCP on penta-PBS for the same full range of rates, simulating one, two, or four penta-OCPs at all combinations of penta-PBS compartments (Fig. 5*D* and *SI Appendix,* Fig. S27). Remarkably, we found that here, too, a quenching rate of 31 ns^{-1} per penta-OCP generated states that closely matched our experimental results across all four states: Q1, Q2, Qa, and Qb, confirming that penta-OCP does indeed quench with the same strength on both tri- and penta-PBS. As with tri-PBS, combinations of two and four penta-OCPs did not strongly differentiate among possible binding sites, but the simulations of monomeric penta-OCP clearly show that only binding at the extra core half-cylinder compartment, E, can produce the Qb state, while binding to either the top or bottom compartment can produce the Qa state. Our experimental observation of both Qa and Qb for the penta-PBS quenched by penta-RCP, thus, leads us to conclude that at least one of the binding sites on the extra core half cylinder (E2, E3, or E5) must be a viable binding site for penta-OCP.

A Binding Model for Penta-OCP on Penta-PBS. Finally, integrating the structural, experimental, and simulated results discussed above, we evaluated all possible combinations of the seven available sites on penta-PBS to determine which pairs might be good candidates for binding dimers of penta-OCP (*SI Appendix,* Tables S3 and S4).

Our evidence had shown that penta-PBS binds as a dimer and that its quenching is similar to that of tri-PBS. Therefore, of the 21 pairs of binding sites evaluated for penta-PBS, we eliminated all combinations that were inconsistent with our experimental and simulation results, i.e., that did not include at least one site on the extra core half cylinder, or pairs that quench the same compartment. We also eliminated all pairs whose spacing fell outside a reasonable range (49 Å < spacing < 97 Å) similar to the known spacing of the T1 and B4 sites on tri-PBS, which are 84.8 Å apart. The remaining candidates after applying these criteria are T1 and E3 (Fig. 5); along with the three pairs shown in *SI Appendix,* Fig. S28: T3 and E5′; B9 and E2; and B9 and E5. Both sites involving B9 seem unlikely, since the B9 site has the largest RMSD from the known OCP-binding motif (2.25 Å). Additionally, both the B9/E5 and T3/E5′ pairs would require substantially different linker orientations within the dimer as compared to the binding configuration in tri-OCP, which has near-C2 symmetry (see *SI Appendix*, Note S5 for additional

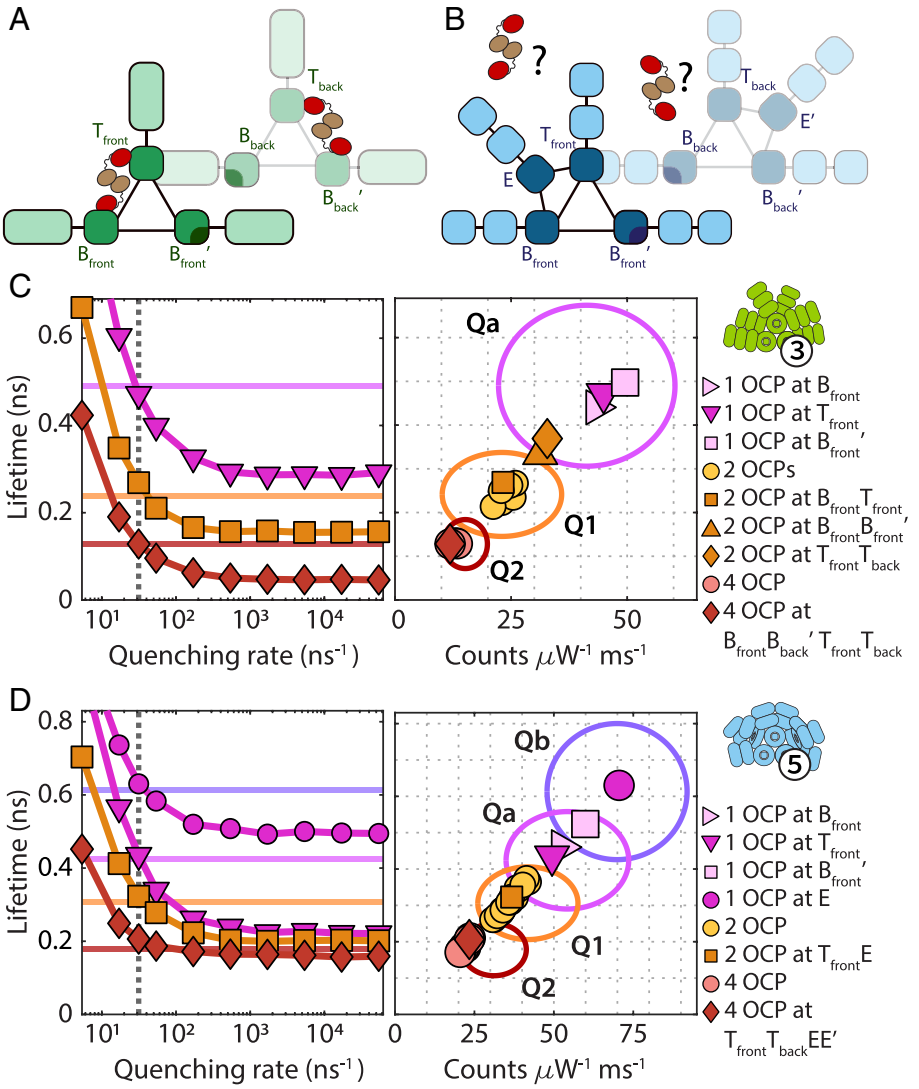

Fig. 5. Photon-by-photon Monte Carlo simulations. A compartmental model for (*A*) quenched tri-PBS and (*B*) quenched penta-PBS was used to simulate the flow of photons through the phycobilisomes using experimentally determined transition rates (40, 41) with and without OCP(s) attached to the different compartments in various combinations. (*C*) *Left:* For tri-PBS quenched at combinations of its known binding sites, either one dimer (orange markers), two dimers (red markers), or one monomer (pink markers) of OCP, the predicted states become more quenched with increasing quenching rate. At a quenching rate of 31 ns^{-1} (vertical dotted line), all three simulated states intersect the experimentally determined Q1 (red horizontal line), Q2 (orange horizontal line), and Qa (pink horizontal line) states, respectively. *Right:* Additional quenching site combinations at an OCP quenching rate of 31 ns^{-1}. (*D*) *Left:* For penta-PBS quenched at selected combinations of the potential binding sites identified earlier in this work, quenching by one dimer (orange markers), two dimers (red markers), or one monomer (pink markers; two different sites shown) of OCP, the predicted states also become more quenched with increasing quenching rate. At a quenching rate of 31 ns^{-1} (vertical dotted line), all four simulated states intersect the experimentally determined Q1 (red horizontal line), Q2 (orange horizontal line), Qa (pink horizontal line), and Qb (purple horizontal line) states, respectively. *Right*: A view of all quenching site combinations at an OCP quenching rate of 31 ns^{-1} shows that only a monomer that is bound to either the top or extra core cylinder can produce states Qa or Qb, respectively.

discussion of linker orientations). Finally, neither the B9 nor T3 sites are bound on tri-PBS despite also being available there. The T1 site, on the other hand, is used in tri-PBS binding with tri-OCP, and both the spacing and linker orientation for the T1/E3 binding site combination match the tri-OCP binding configuration well (spacing 79.5 Å, linkers with near C2 symmetry). Taken altogether, our results therefore support a binding model for penta-OCP on penta-PBS where dimers bind at the T1/E3 sites (Fig. 6).

Discussion

Here, we set out to uncover how structural variations in phycobilisomes, which are formed by the hierarchical assembly of conserved subunits into diverse macromolecular architectures, influence the photoprotective function of OCP. Combining single-particle characterization, numerical simulations, and structural biology data, we identify the photophysical states, and top candidate OCP-interaction sites, associated with OCP–phycobilisome quenching across two cyanobacterial species that exhibit different phycobilisome architectures. Our results, showing that both tri-OCP and penta-OCP quench with similar strength and in the form of one or two dimers, lead us to propose that the quenching mechanism itself is also likely conserved across these species. Specifically, we find that dimeric OCP is responsible for quenching to nearly identical photophysical states Q1 and Q2 in tri- and penta-phycobilisomes but quenches at different sites on each core. We further show that the strength (rate) of OCP quenching is conserved despite asymmetric cross-species binding compatibility, and we identify the most likely candidate binding site pair (T1/E3) on penta-PBS.

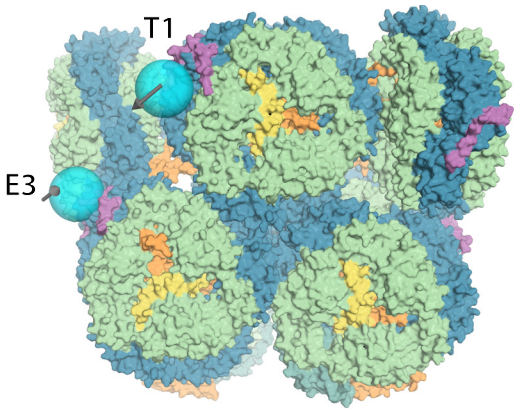

Fig. 6. Potential site for dimeric OCP binding on penta-PBS core. Binding sites where an OCP dimer could feasibly bind are shown as cyan spheres. The arrows on the spheres indicate linker orientation of the aligned N-terminal domain of OCP. The most likely OCP dimer binding location identified in this work is the pair of sites T1 and E3 (dimer spacing: 79.5 Å; linker orientation: 153°).

Future structural studies will be needed to learn why tri-OCP and tri-RCP cannot quench penta-PBS. The OCP sequence and residues in the canonical binding site are conserved between the two core architectures and penta-OCP quenches tri-PBS to photophysical states that are almost indistinguishable from quenching by its native tri-OCP. In particular, the T1 OCP-binding site on the top cylinder of penta-PBS is only slightly different (0.68 Å RMSD) from the closest related known OCP-binding site on tri-PBS, yet even the monomeric tri-RCP did not quench penta-PBS at all. The most likely possibility is that subtle differences in the binding interface preclude a tri-OCP dimer from binding a penta-PBS site. Our related observation that neither tri-RCP nor penta-OCP could achieve the quenched Q1 or Q2 state on tri-PBS (only the less-quenched Qa state), while penta-RCP could quench penta-PBS all the way to the Q2 state, suggests a possible additional influence of dimerization or the C-terminal domain on quenching that may differ across species. Finally, further structural investigation will be able to confirm whether the proposed T1/E3 combination is indeed the correct binding site on penta-PBS.

Overall, we show that the mechanism and strength of OCP1 quenching appear to be conserved across at least some species of cyanobacteria with dissimilar phycobilisome core architectures, indicating that quenching is not necessarily influenced by the higher-order complexity of the phycobilisome. However, the molecular details of the binding site also matter: Despite multiple structurally available binding motifs in both tri- and penta-PBS, OCP binds only at a specific subset of sites in each, and does not bind in identical locations across species. Our work underscores the need for future study of OCP-based photoprotection to fully elucidate how modularity and specificity are balanced in different species and across different phycobilisome architectures. It also lays a foundation for future study of the potentially complex interplay of phycobilisomes with the many OCP homologs that have been identified as well as with other classes of OCP, which may reveal alternative quenching sites or different quenching strength than the OCP1 variants studied here, and for study of the interplay of OCP1 with other accessory proteins such as the fluorescence recovery protein, FRP.

The prevalence of the OCP binding motif on the highly modular phycobilisome may provide a means of conserving OCP function while preserving evolvability of the phycobilisome structure, supporting the evolutionary fitness of species whose phycobilisomes exhibit diverse macromolecular architectures (45). Such design principles may prove useful for artificial light-harvesting technologies, or more broadly for understanding and controlling interactions of macromolecular protein complexes. Together, our findings underscore the exquisite modularity and adaptability of the phycobilisome, and the corresponding specificity and efficiency of OCP quenching that together enable robust photoadaptation by providing a small "fuse" at just the right location.

Materials and Methods

Phycobilisome Purification. Previously established protocols (6, 46) were used to isolate phycobilisomes from *Synechocystis* sp. PCC 6803 and *Anabaena* sp. PCC 7120. Briefly, cyanobacteria were grown photoautotrophically in BG11 medium at 30 °C and with 3% CO_2. The cells were collected by centrifugation (8,000 rpm; 10 min) and washed with 0.8 M phosphate buffer, pH 7.5. After centrifugation, the pellet was resuspended in 0.8 M phosphate buffer containing protease inhibitor and 10 units/ml of DNase I. The cells were broken by passing through a French press twice at 1,000 psi. Broken cells were incubated with 1% v/v Triton X for 15 min while shaking under the dark. Cellular debris was removed by centrifuging at 30,000×*g* for 15 min. The supernatant was collected and centrifuged again at 42,000 rpm for 1 h. The supernatant was added to a discontinuous sucrose gradient containing layers of 1.5, 1.0, 0.75, 0.5, and 0.25 M sucrose in 0.75 M phosphate buffer and centrifuged overnight at 25,000 rpm in a swinging bucket rotor. Intact phycobilisomes were collect at the interface of 0.75 and 1.0 M sucrose layer.

OCP Purification and Activation. The OCPs from *Synechocystis* sp. PCC 6803 and *Anabaena* sp. PCC 7120 were expressed in *Escherichia coli* as described previously (17). Briefly, the sequence for a C-terminal histidine tag and the *Synechocystis* sp. PCC 6803 *ocp* gene (*slr1963*) were cloned into pCDFDuet (Novagen). Similarly, the *Anabaena* sp. PCC 7120 *ocp* gene (*all3149*) along with a C-terminal histidine tag were cloned into pET28a (Novagen). The resulting plasmids were expressed in BL21 (DE3) along with the plasmid pAC-CANthipi [Addgene (47)] to obtain the canthaxanthin-containing OCPs. The proteins were purified via affinity chromatography (HisTrap HP, GE Healthcare) and hydrophobic interaction chromatography (HiTrap Phenyl HP, GE Healthcare) to yield the holo-OCP. Purified OCPs were activated using a 488 nm laser (Coherent OBIS 1220123; 10 min; ~1 μmol photons s^{-1} cm^{-2}).

Converting OCP Into the Permanently Active RCP. We cleaved the linker connecting the N-terminal domain (NTD) and the C-terminal domain (CTD) of the OCP to create the permanently active RCP. To cleave the OCP linker, we used trypsin digestion (Promega V5111) following the method from Leverenz et al (8). Briefly, trypsin was added to activated OCP with a protease:protein ratio of 1:150. Protein digestion was allowed to proceed for 20 min under the 488 nm laser illumination. Then, phenylmethylsulfonyl fluoride was added to a final concentration to 1 mM to quench the reaction.

Phycobilisome Quenching Assay. OCP or RCP was mixed with purified phycobilisomes in excess. The mixture was incubated on ice (in the dark) for 10 min and diluted to ~ 25 to 100 pM prior to trapping. When titrating with OCP (*SI Appendix*, Fig. S20), we reduced the relative amount of OCP during incubation. For RCP titration experiments (Fig. 3), excess RCP was present during incubation. Since RCP unbinds at the low concentrations needed for single-molecule measurements (*SI Appendix*, Fig. S23), varying amounts of RCP (as shown in Fig. 3) were present in the sample during measurement. A 1 M phosphate buffer (pH 7.4) with 1 M sucrose was used for binding and single-molecule measurements.

Single-Molecule Measurements. The ABEL trap was implemented similar to previous iterations (36, 37). Briefly, an acousto-optic tunable filter (Leukos TANGO VIS) paired with a pulsed supercontinuum laser (Leukos ROCK 400-4) and a pulse picker (Conoptics M350-160-01 KD*P EOM) were used to select 594 nm at 30.1 MHz repetition rate as the excitation source. The excitation laser was passed through two orthogonally placed AODs (MTT110-B50A1.5-VIS) and relayed to the back of the microscope and reflected by a dichroic (Di03-R594-t3-25 × 36) toward the objective (Olympus UPLSAPO100XS). The fluorescence from a trapped molecule passed through the microscope dichroic, a 300 μm pinhole, and the emission filters (Semrock

FF01-650/150-25 and NF03-594E-25) and was split using a dichroic (T660lpxr) into red and green channels and detected by two APDs (Excelitas SPCM-AQRH-14-ND). Upon detecting a photon, the APDs send a signal to the TCSPC (Picoquant Multiharp 150) and an FPGA (National Instruments PCIe-7856) to provide feedback. The FPGA calculates the required voltages in the X and Y directions and sends them to two voltage amplifiers (Pendulum F10AD) which apply the voltage to the sample through four platinum electrodes placed orthogonally in a microfluidic chip.

Microfluidic Cell Preparation. The microfluidic cells were prepared in-house as previously described (48). Routine photolithography techniques were used to etch the trapping region with ~700 nm depth and surrounding channels with a depth of 12 μm (*SI Appendix*, Fig. S9). The microfluidic cells were permanently bonded to quartz coverslips using 6% sodium silicate solution (SIGMA 338443) following a procedure adapted from ref. 49. The cells were cleaned and reused indefinitely.

Prior to each trapping experiment, the microfluidic cells were cleaned in piranha (3:1 mixture of sulfuric acid and hydrogen peroxide) overnight. Then, the cells were incubated in 1 M KOH for 10 min and rinsed thoroughly. To prevent protein from sticking to the cell walls, we passivated the cells using polyelectrolyte multilayers. First, the cells were incubated in 0.5 wt. % poly(ethyleneimine) solution (Sigma Aldrich 181978) for 10 min. The cells were rinsed twice and incubated in 0.5 wt. % poly(acrylic acid, sodium salt) solution (Sigma Aldrich 416010) for 10 min. These two steps were repeated one more time. The cells were rinsed with ultrapure water before adding the sample for trapping.

Data Analysis. All data analysis was performed in MATLAB. The time-tagged photon data from the TCSPC were used to construct 10-ms binned brightness traces. An established change-point finding algorithm (50) was used to find levels of constant brightness within each trace. Each level was divided into 500-photon groups to calculate brightness, lifetime for both channels (51, 52), and red ratio. The red ratio is defined as

$$\text{Red ratio} = \frac{I_{red}}{I_{red} + I_{green}},$$

where I_{red} is the background subtracted intensity of the red channel (emission photons over 660 nm) and I_{green} is the background subtracted intensity of the green channel (emission photons below 660 nm). See *SI Appendix*, Fig. S10 for additional details on the red ratio.

All reported brightness values were normalized by dividing by the measured excitation intensity before the microscope objective. Lifetimes for single-molecule data were fitted using single exponential fits convolved with the instrument response function (IRF) determined using a low fluorescence lifetime dye, malachite green. For each 500-photon group, pairs of calculated photophysical parameters were plotted as 2-D scatter heatmaps where each point is colored according to the relative density of neighboring points, as shown in Figs. 2 and 3.

Additional details of protein sequence analysis and data analysis are provided in *SI Appendix*, Notes S1 and S2.

Energy Transfer Simulations. A detailed description of the Monte Carlo simulations of energy transfer in unquenched and quenched phycobilisomes is provided in *SI Appendix*, Note S4.

Data, Materials, and Software Availability. Source data supporting the findings of this study are available via the Zenodo repository at https://doi.org/10.5281/zenodo.16973966 (53).

ACKNOWLEDGMENTS. A.H.S. acknowledges support from the Early Career Award from the Office of Science of the US Department of Energy (DE-SC0025385), as well as support from NSF Quantum Leap Challenge Institute Quantum Sensing for Biophysics and Bioengineering Grant OMA-2121044 and from the Neubauer Family Foundation. C.A.K. acknowledges research support from the Office of Science of the US Department of Energy (DE-SC0020606). We thank Dr. Anupama Puppala and Prof. Greg Engel for helpful feedback and Dr. Karen Watters for assistance with technical writing and editing.

Author affiliations: [a]Department of Chemistry, University of Chicago, Chicago, IL 60637; [b]Michigan State University - Department of Energy (MSU–DOE) Plant Research Laboratory, Michigan State University, East Lansing, MI 48824; [c]Environmental Genomics and Systems Biology Division, Lawrence Berkeley National Laboratory, Berkeley, CA 94720; [d]Molecular Biophysics and Integrated Bioimaging Division, Lawrence Berkeley National Laboratory, Berkeley, CA 94720; [e]Department of Biochemistry and Molecular Biology, Michigan State University, East Lansing, MI 48824; [f]Pritzker School of Molecular Engineering, University of Chicago, Chicago, IL 60637; [g]Institute for Biophysical Dynamics, University of Chicago, Chicago, IL 60637; [h]James Franck Institute, University of Chicago, Chicago, IL 60637; and [i]Chan-Zuckerberg Biohub Chicago, Chicago, IL 60642

Author contributions: A.E., C.A.K., and A.H.S. designed research; A.E. and M.S. performed research; A.E. and S.L.-Y. contributed new reagents/analytic tools; A.E., M.S., and A.H.S. analyzed data; and A.E. and A.H.S. wrote the paper with input from all authors.

1. T. Platt, D. V. S. Rao, B. Irwin, Photosynthesis of picoplankton in the oligotrophic ocean. *Nature* **301**, 702–704 (1983).
2. H. L. MacIntyre, R. J. Geider, D. C. Miller, Microphytobenthos: The ecological role of the "secret garden" of unvegetated, shallow-water marine habitats. i. distribution, abundance and primary production. *Estuaries* **19**, 186 (1996).
3. W. B. Whitman, D. C. Coleman, W. J. Wiebe, Prokaryotes: The unseen majority. *Proc. Natl. Acad. Sci. U.S.A.* **95**, 6578–6583 (1998).
4. R. E. Blankenship, *Molecular Mechanisms of Photosynthesis, Second Edition* (Wiley/Blackwell, 2014).
5. A. Wilson *et al.*, A soluble carotenoid protein involved in phycobilisome-related energy dissipation in cyanobacteria. *Plant Cell* **18**, 992–1007 (2006).
6. M. Gwizdala, A. Wilson, D. Kirilovsky, In vitro reconstitution of the cyanobacterial photoprotective mechanism mediated by the orange carotenoid protein in *Synechocystis* PCC 6803. *Plant Cell* **23**, 2631–2643 (2011).
7. D. Jallet *et al.*, Specificity of the cyanobacterial orange carotenoid protein: Influences of Orange Carotenoid Protein and phycobilisome structures. *Plant Physiol.* **164**, 790–804 (2014).
8. R. L. Leverenz *et al.*, Structural and functional modularity of the Orange Carotenoid Protein: Distinct roles for the N- and C-terminal domains in cyanobacterial photoprotection. *Plant Cell* **26**, 426–437 (2014).
9. R. López-Igual *et al.*, Different functions of the paralogs to the N-terminal domain of the Orange Carotenoid Protein in the cyanobacterium *Anabaena* sp. PCC 7120. *Plant Physiol.* **171**, 1852–1866 (2016).
10. N. N. Sluchanko *et al.*, Structural framework for the understanding spectroscopic and functional signatures of the cyanobacterial orange carotenoid protein families. *Int. J. Biol. Macromol.* **254**, 127874 (2024).
11. N. Adir, S. Bar-Zvi, D. Harris, The amazing phycobilisome. *Biochimica et Biophysica Acta (BBA)* **1861**, 148047 (2020).
12. R. MacColl, Cyanobacterial phycobilisomes. *J. Struct. Biol.* **124**, 311–334 (1998).
13. N. Adir, Elucidation of the molecular structures of components of the phycobilisome: Reconstructing a giant. *Photosynth. Res.* **85**, 15–32 (2005).
14. J. Zhang *et al.*, Structure of phycobilisome from the red alga *Griffithsia pacifica*. *Nature* **551**, 57–63 (2017).
15. J. Ma *et al.*, Structural basis of energy transfer in *Porphyridium purpureum* phycobilisome. *Nature* **579**, 146–151 (2020).
16. L. Zheng *et al.*, Structural insight into the mechanism of energy transfer in cyanobacterial phycobilisomes. *Nat. Commun.* **12**, 5497 (2021).
17. M. A. Domínguez-Martín *et al.*, Structures of a phycobilisome in light-harvesting and photoprotected states. *Nature* **609**, 835–845 (2022).
18. X. Zhang, Y. Xiao, X. You, S. Sun, S.-F. Sui, In situ structural determination of cyanobacterial phycobilisome–PSII supercomplex by STAgSPA strategy. *Nat. Commun.* **15**, 7201 (2024).
19. L. Chang *et al.*, Structural organization of an intact phycobilisome and its association with photosystem II. *Cell Res.* **25**, 726–737 (2015).
20. M. Watanabe, M. Ikeuchi, Phycobilisome: Architecture of a light-harvesting supercomplex. *Photosynth. Res.* **116**, 265–276 (2013).
21. F. Muzzopappa, D. Kirilovsky, Changing color for photoprotection: The orange carotenoid protein. *Trends Plant Sci.* **25**, 92–104 (2020).
22. C. Boulay, L. Abasova, C. Six, I. Vass, D. Kirilovsky, Occurrence and function of the orange carotenoid protein in photoprotective mechanisms in various cyanobacteria. *Biochim. Biophys. Acta BBA - Bioenerg.* **1777**, 1344–1354 (2008).
23. C. A. Kerfeld *et al.*, The crystal structure of a cyanobacterial water-soluble carotenoid binding protein. *Structure* **11**, 55–65 (2003).
24. S. Bandara *et al.*, Photoactivation mechanism of a carotenoid-based photoreceptor. *Proc. Natl. Acad. Sci.* **114**, 6286–6291 (2017).
25. P. V. Sauer *et al.*, Structural and quantum chemical basis for OCP-mediated quenching of phycobilisomes. *Sci. Adv.* **10**, eadk7535 (2024).
26. E. G. Maksimov *et al.*, The time course of non-photochemical quenching in phycobilisomes of Synechocystis sp. PCC6803 as revealed by picosecond time-resolved fluorimetry. *Biochim. Biophys. Acta BBA - Bioenerg.* **1837**, 1540–1547 (2014).
27. D. Jallet, M. Gwizdala, D. Kirilovsky, ApcD, ApcF and ApcE are not required for the Orange Carotenoid Protein related phycobilisome fluorescence quenching in the cyanobacterium Synechocystis PCC 6803. *Biochim. Biophys. Acta BBA - Bioenerg.* **1817**, 1418–1427 (2012).
28. I. N. Stadnichuk *et al.*, Electronic coupling of the phycobilisome with the orange carotenoid protein and fluorescence quenching. *Photosynth. Res.* **124**, 315–335 (2015).
29. M. Gwizdala *et al.*, Switching an individual phycobilisome off and on. *J. Phys. Chem. Lett.* **9**, 2426–2432 (2018).
30. A. H. Squires *et al.*, Single-molecule trapping and spectroscopy reveals photophysical heterogeneity of phycobilisomes quenched by orange carotenoid protein. *Nat. Commun.* **10**, 1172 (2019).

31. M. Golub *et al.*, Solution structure and conformational flexibility in the active state of the Orange Carotenoid Protein: Part I. Small-angle scattering. *Small-Angle Scattering. J. Phys. Chem. B* **123**, 9525–9535 (2019).
32. E. A. Andreeva *et al.*, Oligomerization processes limit photoactivation and recovery of the orange carotenoid protein. *Biophys. J.* **121**, 2849–2872 (2022).
33. M. Golub *et al.*, Stages of OCP–FRP interactions in the regulation of photoprotection in cyanobacteria, Part 2: Small-angle neutron scattering with partial deuteration. *J. Phys. Chem. B* **127**, 1901–1913 (2023).
34. T. Tokashiki *et al.*, Kinetic Insights into Photoinduced Monomer–Dimer Conversion and Activation of Orange Carotenoid Protein. biorXiv [Preprint] (2025), http://biorxiv.org/lookup/doi/10.1101/2025.05.26.656073 [Accessed 9 July 2025].
35. R. H. Goldsmith, W. E. Moerner, Watching conformational-and photodynamics of single fluorescent proteins in solution. *Nat. Chem.* **2**, 179–186 (2010).
36. Q. Wang, W. E. Moerner, Dissecting pigment architecture of individual photosynthetic antenna complexes in solution. *Proc. Natl. Acad. Sci. U.S.A.* **112**, 13880–13885 (2015).
37. A. H. Squires, W. Moerner, Direct single-molecule measurements of phycocyanobilin photophysics in monomeric C-phycocyanin. *Proc. Natl. Acad. Sci. U.S.A.* **114**, 9779–9784 (2017).
38. M. Gwizdala, R. Berera, D. Kirilovsky, R. van Grondelle, T. P. J. Krüger, Controlling light harvesting with light. *J. Am. Chem. Soc.* **138**, 11616–11622 (2016).
39. T. P. J. Krüger, R. van Grondelle, M. Gwizdala, The role of far-red spectral states in the energy regulation of phycobilisomes. *Biochim. Biophys. Acta BBA - Bioenerg.* **1860**, 341–349 (2019).
40. I. H. M. van Stokkum *et al.*, A functional compartmental model of the Synechocystis PCC 6803 phycobilisome. *Photosynth. Res.* **135**, 87–102 (2018).
41. A. Biswas, X. Huang, P. H. Lambrev, I. H. M. van Stokkum, Modelling excitation energy transfer and trapping in the filamentous cyanobacterium Anabaena variabilis PCC 7120. *Photosynth. Res.* **144**, 261–272 (2020).
42. A. E. Cohen, W. Moerner, Suppressing brownian motion of individual biomolecules in solution. *Proc. Natl. Acad. Sci. U.S.A.* **103**, 4362–4365 (2006).
43. A. H. Squires, A. E. Cohen, W. E. Moerner, "Anti-Brownian Traps" in *Encyclopedia of Biophysics, European Biophysical Societies*, G. Roberts, A. Watts, Eds. (Springer, Berlin Heidelberg, 2018), pp. 1–8.
44. C. A. Kerfeld, M. R. Melnicki, M. Sutter, M. A. Dominguez-Martin, Structure, function and evolution of the cyanobacterial orange carotenoid protein and its homologs. *New Phytol.* **215**, 937–951 (2017).
45. G. P. Wagner, M. Pavlicev, J. M. Cheverud, The road to modularity. *Nat. Rev. Genet.* **8**, 921–931 (2007).
46. W. Lou, D. M. Niedzwiedzki, R. J. Jiang, R. E. Blankenship, H. Liu, Binding of red form of Orange Carotenoid Protein (OCP) to phycobilisome is not sufficient for quenching. *Biochim. Biophys. Acta BBA - Bioenerg.* **1861**, 148–155 (2020).
47. F. X. Cunningham, E. Gantt, A portfolio of plasmids for identification and analysis of carotenoid pathway enzymes: Adonis aestivalis as a case study. *Photosynth. Res.* **92**, 245–259 (2007).
48. A. E. Cohen, W. E. Moerner, *An All-glass Microfluidic Cell for The ABEL Trap: Fabrication and Modeling*, K. Dholakia, G. C. Spalding, Eds. (2005), p. 59300S.
49. H. Y. Wang, R. S. Foote, S. C. Jacobson, J. H. Schneibel, J. M. Ramsey, Low temperature bonding for microfabrication of chemical analysis devices. *Sens. Actuators, B Chem.* **45**, 199–207 (1997).
50. L. P. Watkins, H. Yang, Detection of intensity change points in time-resolved single-molecule measurements. *J. Phys. Chem. B* **109**, 617–628 (2005).
51. C. Zander *et al.*, Detection and characterization of single molecules in aqueous solution. *Appl. Phys. B Laser Opt.* **63**, 517–523 (1996).
52. L. Brand, C. Eggeling, C. Zander, K. H. Drexhage, C. A. M. Seidel, Single-molecule identification of coumarin-120 by time-resolved fluorescence detection: Comparison of one- and two-photon excitation in solution. *J. Phys. Chem. A* **101**, 4313–4321 (1997).
53. A. Ejaz, M. Sutter, S. Lechno-Jossef, C. A. Kerfeld, A. H. Squires, "Phycobilisome core architecture influences photoprotective quenching by the Orange Carotenoid Protein." Zenodo. https://doi.org/10.5281/zenodo.16973966. Deposited Deposited 9 September 2025.